Chemical Science

ROYAL SOCIETY OF CHEMISTRY

EDGE ARTICLE

View Article Online
View Journal | View Issue

Check for updates

Cite this: *Chem. Sci.*, 2025, **16**, 14793

All publication charges for this article have been paid for by the Royal Society of Chemistry

Amino-induced cleavage of the electron-communicating S-bridge to unlock mixed-valence copper for potent oxidase-like catalysis and selective sensing†

Bojin Li,[a] Nannan Xia,[b] Chaofeng Huang,*[c] Xun Hu *[a] and Fei He *[a]

Transition-metal sites with mixed valence often coexist in diverse catalysts, yet their precise roles remain elusive. Taking a thiadiazole-coordinated Cu nanozyme system as an example, we developed ligand side-group engineering to modulate adjacent dicopper sites with different mixed Cu^{1+}/Cu^{2+} states. Amino functionalization of the ligand induced the cleavage of the electron-communicating S-bridge connecting adjacent copper centers, allowing precise manipulation of the ratio of mixed Cu^{1+}/Cu^{2+} sites. Such a tailored mixed-valence composition accelerated the preferential and selective activation of O_2 to $O_2^{\bullet-}$ through the synergistical mechanism of Cu^{2+}-dominated adsorption of O_2 and Cu^{1+}-controlled electron transfer in the initial catalysis step. This targeted pathway boosted the oxidase-mimicking activity of the mixed-valence nanozyme nearly 85-fold compared to its counterpart with adjacent S-bridged Cu centers. The outstanding oxidase-like activity, coupled with the unique affinity of mixed Cu^{1+}/Cu^{2+} sites for phosphorus, further enabled the highly selective and sensitive sensing of cytotoxic tris(2-carboxyethyl)phosphine with a 0.96-ppm detection limit *via* a complexation-dominated activity inhibition mechanism. This fundamental insight into the mixed-valence synergy of metal sites provided a new perspective for designing efficient catalysts for various purposes, such as catalysis, sensing and more.

Received 15th May 2025
Accepted 4th July 2025

DOI: 10.1039/d5sc03521j

rsc.li/chemical-science

Open Access Article. Published on 05 July 2025. Downloaded on 5/4/2026 11:46:44 PM.
This article is licensed under a Creative Commons Attribution-NonCommercial 3.0 Unported Licence.

Introduction

The electronic states of transition-metal centers often dictate their catalytic activities through governing elementary steps vital for biomimetic catalysis,[1] energy conversion,[2] and catalytic sensing.[3] Intriguingly, many catalysts operate not through metals in a single oxidation state, but rather through mixed-valence metal sites, which often influence the catalytic activity of catalysts, particularly in multi-electron redox reactions like oxygen activation.[4,5] Taking nanozymes with mixed-valence Cu^{1+}/Cu^{2+} as an example, conflicting initial O_2 activation species (*e.g.*, the selective generation of $O_2^{\bullet-}$ *vs.* O_2^{2-} or even $^1O_2$) are seen at adjacent multicopper sites and correspondingly disparate oxidase-mimicking activities are frequently observed.[5–7] However, the specific roles of each valence state and potential synergistic effects in O_2 activation remain elusive. This is due to a lack of well-defined molecular platforms with precisely engineered adjacent Cu sites, where the valence state distribution can be systematically controlled. As a result, the rational design of Cu-based oxidase-mimicking nanozymes with precisely tailored activity remains challenging.

To address this challenge, we developed a novel strategy centered on the ligand side-group-induced cleavage of an electron-communicating S-bridge which connected adjacent copper centers within a thiadiazole-coordinated nanozyme system. We demonstrated that the installation of an amino functional group on the ligand induced the S-bridge cleavage of the Cu···S···Cu linkage. Such cleavage modulated the ratio of mixed-valence Cu^{1+}/Cu^{2+} sites, creating a system dominated by spatially proximal but electronically distinct dicopper centers. Accordingly, this adjacent Cu^{1+}/Cu^{2+} unlocked a potent synergistic pathway for O_2 activation during mimicking oxidase-like oxidation. Through cooperative action, the Cu^{2+} site preferentially bonded with O_2 while the adjacent Cu^{1+} site facilitated rapid electron transfer to O_2, thus leading to the selective and accelerated formation of $O_2^{\bullet-}$ as the key initial reactive oxygen species. This dramatically boosted the intrinsic oxidase-like activity of the mixed-valence nanozyme nearly 85-fold compared to its S-bridged counterpart. Beyond catalysis, the unique electronic signature of the proximal Cu^{1+}/Cu^{2+} pair

[a]School of Material Science and Engineering, University of Jinan, Jinan 250024, China. E-mail: xun.hu@outlook.com; mse_hef@ujn.edu.cn

[b]State Key Laboratory of Green Papermaking and Resource Recycling, Key Laboratory of Pulp & Paper Science and Technology of Shandong Province/Ministry of Education, Qilu University of Technology (Shandong Academy of Sciences), Jinan 250353, China

[c]School of Chemistry and Chemical Engineering/State Key Laboratory Incubation Base for Green Processing of Chemical Engineering, Shihezi University, Shihezi 832000, China. E-mail: cf.huang@shzu.edu.cn

† Electronic supplementary information (ESI) available. See DOI: https://doi.org/10.1039/d5sc03521j

© 2025 The Author(s). Published by the Royal Society of Chemistry

Open Access Article. Published on 05 July 2025. Downloaded on 5/4/2026 11:46:44 PM. This article is licensed under a Creative Commons Attribution-NonCommercial 3.0 Unported Licence.

showed affinity towards cytotoxic tris(2-carboxyethyl) phosphine, thereby enabling the highly selective sensing of TCEP with a low detection limit of 0.96 ppm *via* a complexation-dominated inhibition mechanism.

Results and discussion

To construct the adjacent dicopper centers, two heterocyclic ligands (*i.e.*, 2-mercapto-1,3,4-thiadiazol (MTD) and 2-amino-5-mercapto-1,3,4-thiadiazole (AMTD)) were chosen due to the existence of two neighboring heterocyclic N atoms in each of them, which were capable of coordinating with Cu to control the distance between dicopper atoms (Schemes 1 and S1†). After the two thiadiazol ligands were stirred with $CuSO_4$ in DMF/H_2O solution for 24 h, respectively, the produced precipitates were collected through centrifugation. These precipitates were further washed and dried to obtain the resulting Cu-based nanozymes, labelled as Cu-MTD and Cu-AMTD (see Experimental section in the ESI†).

According to scanning electron microscope (SEM) images, aggregated nanoparticles with an average size of 48.8 nm were obviously observed for Cu-MTD (Fig. 1A), corresponding with the transmission electron microscope (TEM) results (Fig. S1†). Similarly, Cu-AMTD also presented an aggregated nanoparticle morphology in SEM and TEM images (Fig. 1B and C), but the size of these nanoparticles seemed to be irregular compared with that of Cu-MTD. Energy dispersive spectroscopy (EDS) mapping displayed that Cu and the other four elements (*i.e.*, C, N, O, and S) were uniformly dispersed in both Cu-AMTD and Cu-MTD without obvious aggregation (Fig. 1D and S2†), implying that Cu probably existed in the form of an atomic dispersion. Moreover, the Cu content levels in Cu-AMTD and Cu-MTD were determined to be 33.1% and 40.9%, respectively, according to inductively coupled plasma optical emission spectrometry (ICP-OES) (Fig. S3 and S4†).

In the XRD patterns, we found that both Cu-MTD and Cu-AMTD presented two similar broad and weak diffraction signals (Fig. S5A†), implying the polymeric or highly disordered nature of these materials. In addition, few highly orderly lattice fringes were found for AMTD and Cu-MTD in high-resolution transmission electron microscopy (Fig.S5B and S5C†), further indicating their polymeric or highly disordered nature.

X-ray photoelectron spectroscopy (XPS) was carried out to further investigate the surface element compositions and electronic states of Cu-AMTD and Cu-MTD. In the N 1s spectrum, only one Cu–N peak was observed for Cu-MTD (Fig. 2A),

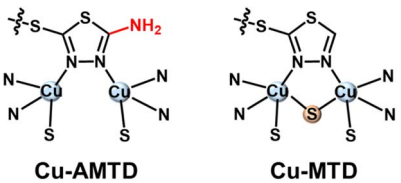

Scheme 1 Simplified coordination configurations of the atomic Cu sites in Cu-MTD and Cu-AMTD.

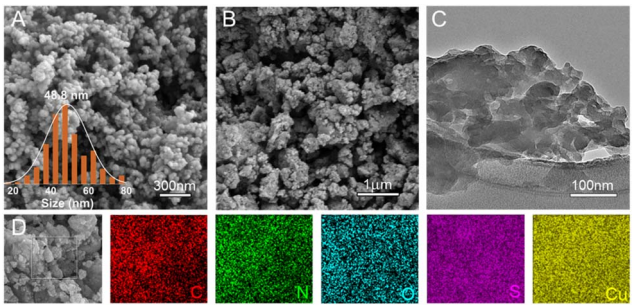

Fig. 1 SEM images of Cu-MTD (A) and Cu-AMTD (B). A TEM image (C) and EDS mapping (D) of Cu-AMTD.

indicating that both of the heterocyclic N atoms coordinated with Cu. Unlike Cu-MTD, two peaks, corresponding to Cu–N and C–NH_2, existed for Cu-AMTD (Fig. 2A). The area ratio of Cu–N to C–NH_2 approached 2, signifying that coordination occurred between Cu and the two heterocyclic N atoms rather than exocyclic –NH_2.[8] In addition to Cu–N, Cu–S coordination was also found for both Cu-AMTD and Cu-MTD (Fig. 2B), illustrating that the S atoms of AMTD and MTD tended to coordinate with Cu. Due to the stronger coordination potential of S atoms in –SH compared with thiophene S atoms, the Cu–S bond possibly stemmed from coordination effects between –SH and Cu.[9]

Importantly, though both Cu-AMTD and Cu-MTD showed Cu–N and Cu–S coordination, their Cu 2p spectra showed

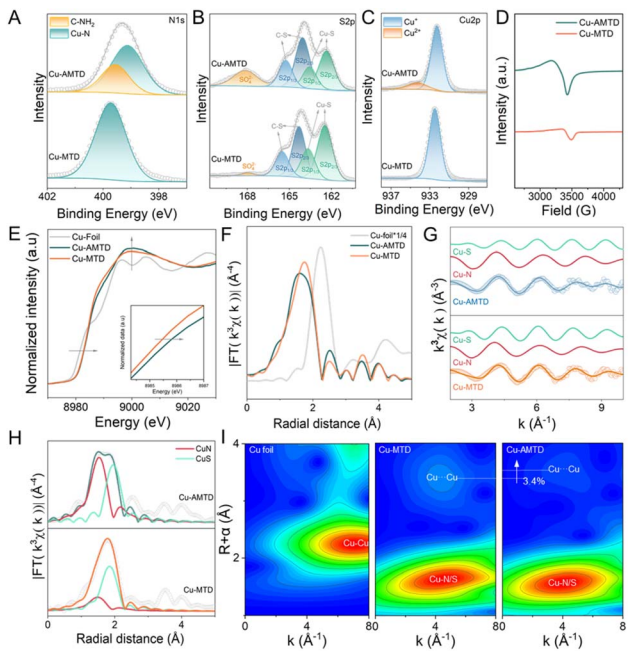

Fig. 2 Coordination configurations and electronic structures of Cu-AMTD and Cu-MTD. N 1s (A), S 2p (B) and Cu 2p (C) XPS spectra; EPR spectra of Cu-AMTD and Cu-MTD (D); Cu K-edge XANES spectra (E), Fourier-transform EXAFS curves in *R*-space (F) and *k*-space (G), Fourier-transform EXAFS fitting curves in *k*-space (H) and wavelet-transform EXAFS spectra (I).

© 2025 The Author(s). Published by the Royal Society of Chemistry

Open Access Article. Published on 05 July 2025. Downloaded on 5/4/2026 11:46:44 PM. This article is licensed under a Creative Commons Attribution-NonCommercial 3.0 Unported Licence.

obvious differences. As seen in Fig. 2C, we found that only Cu^{1+} existed in Cu-MTD. However, Cu-AMTD contained mixed Cu^{1+}/Cu^{2+} species. The appearance of Cu^{1+} species in Cu-AMTD and Cu-MTD was mainly attributed to the reducing property of the –SH group and heterocyclic N atoms in AMTD and MTD.[10,11] Given that the existence of extra $-NH_2$ was the only difference between MTD and AMTD, we deduced that $-NH_2$ in AMTD probably triggered an inductive effect to modulate the Cu–N and Cu–S coordination number, thus causing the formation of mixed Cu^{1+}/Cu^{2+} species.

The electron paramagnetic resonance (EPR) spectrum also supported the existence of Cu^{2+} in Cu-AMTD (Fig. 2D). It should be noted that a much weaker Cu^{2+} signal was also observed for Cu-MTD. However, the Cu 2p XPS spectrum did not show the existence of Cu^{2+} in Cu-MTD. Such a phenomenon was attributed to the reduction of Cu^{2+} to Cu^{1+} when Cu-MTD was exposed to X-rays during XPS analysis. The short exposure time (~2 min) for both Cu-MTD and Cu-AMTD meant that the amount of reduction of Cu^{2+} to Cu^{1+} was rather small.[12] However, the finally obtained Cu 2p spectra showed that Cu^{2+} was still observed for Cu-AMTD and Cu^{2+} was not found for Cu-MTD. Such a result, together with the EPR results, further reflected that the Cu^{2+} content in Cu-AMTD was obviously higher, and the Cu^{2+} content in Cu-MTD was rather low. Accordingly, the Cu^{+} content in Cu-MTD was higher than that in Cu-AMTD. These results indicated that introducing $-NH_2$ into the ligand contributed to modulating the ratio of mixed-valence copper.

To further determine the electronic states and atomic-scale coordination configurations of Cu in Cu-MTD and Cu-AMTD, Cu K-edge X-ray absorption near-edge structure (XANES) spectra were collected. Compared with Cu foil, both Cu-MTD and Cu-AMTD presented higher pre-edge absorption energies (Fig. 2E), indicating that Cu was in an oxidated state. The pre-edge absorption energy of Cu-AMTD shifted positively, and the peak intensity of the white line corresponding to the $1s \rightarrow 4p_{xy}$ transition also rose compared with that of Cu-MTD (Fig. 2E), suggesting the higher average chemical valence of Cu in Cu-AMTD. Such a result was consistent with the Cu 2p and EPR spectra, which showed that the Cu^{2+} content in Cu-AMTD was higher than that in Cu-MTD.

Apart from the positively shifted Cu K-edge pre-edge absorption energy, Cu-AMTD also presented a negatively shifted binding energy of the Cu–N bond compared with Cu-MTD (Fig. 2A). These results, together with the fact that some Cu^{2+} in $CuSO_4$ was transformed into Cu^{1+} species in Cu-MTD and Cu-AMTD, indicated that fewer electrons from the coordinating heterocyclic N atoms in AMTD were transferred to Cu compared to those in MTD. Such a phenomenon was attributed to an induction effect triggered by p–π conjugation between $-NH_2$ and the thiadiazole ring in AMTD, which reduced the flow of electrons from AMTD to Cu.

In the extended X-ray absorption fine structure (EXAFS) spectra in *R* space, Cu-MTD and Cu-AMTD showed characteristic scattering peaks at ~1.60 and 1.75 Å, and no Cu–Cu scattering peak at ~2.24 Å was observed (Fig. 2F). This signified the atomic dispersion of Cu in both Cu-MTD and Cu-AMTD. Importantly, the characteristic scattering peak intensity of Cu-AMTD was weaker than that of Cu-MTD, suggesting a possible lower N/S coordination number around Cu in Cu-AMTD. According to the Fourier-transform EXAFS signal in *k*-space, two different oscillation periods corresponding to Cu–N and Cu–S paths were observed for both Cu-MTD and Cu-AMTD (Fig. 2G), which favored the formation of Cu–N and Cu–S coordination, as shown by the N 1s/S 2p spectra (Fig. 2A and B). To determine the first-shell N/S coordination numbers around the Cu center, Fourier-transform EXAFS fitting analysis in *R* space was conducted. Fig. 2H and Table S1† show that each Cu center in Cu-MTD bonded with three N atoms, and the average number of coordinated S atoms approached 1.5, which suggested that three S atoms were shared by two adjacent Cu atoms. This signified that Cu-MTD formed a CuN_3S_2 coordination configuration, and the adjacent dicopper atoms were connected by one S bridge. For Cu-AMTD, the average number of coordinated N and S atoms around the Cu center approached 3 and 1, respectively, thus forming a low-coordinated CuN_3S_1 configuration. This could be supported by the weaker scattering peak intensity of Cu-AMTD in Fig. 2F, and implied the cleavage of the S-bridge between adjacent dicopper centers.

Importantly, after the S bridge between the two adjacent Cu atoms was disrupted, the ratio of mixed Cu^{1+}/Cu^{2+} species changed in Cu-AMTD, according to the Cu 2p and EPR spectra (Fig. 2C and D). However, once the S bridge was formed, the adjacent dual-atomic Cu in Cu-MTD presented a higher Cu^{1+} content. This implied the electronic communication function of the S bridge between the adjacent dual-atomic Cu centers, which flexibly modulated the electronic states of the Cu centers. Moreover, the presence of more Cu^{2+} meant an increased positive charge density for Cu in Cu-AMTD, which theoretically caused stronger charge repulsion between adjacent Cu^{1+} and Cu^{2+} in Cu-AMTD compared with in Cu-MTD.[13] This would increase the distance between the adjacent dicopper centers in Cu-AMTD. In wavelet transform (WT)-EXAFS spectra (Fig. 2I), we obviously observed that the distance between the adjacent dual-atomic Cu centers in Cu-AMTD increased compared with the S-bridge-locked dicopper centers in Cu-MTD, in accordance with the above speculation.

These distinct coordination configurations and electronic states of Cu-MTD and Cu-AMTD, as well as the structural differences between MTD and AMTD, illustrated that introducing the $-NH_2$ group into the ligand was prone to induce the cleavage of the electron-communicating S-bridge between adjacent Cu atoms. This modulated the ratio of mixed Cu^{1+}/Cu^{2+} species, thus controlling the asymmetric charge distribution over the neighbouring low-coordinated dicopper centers. On the contrary, the absence of $-NH_2$ in the ligand enabled the formation of an S-bridge in Cu-MTD, which promoted charge redistribution between the adjacent dual-atomic Cu centers by enhancing electronic communication. As a result, this produced more Cu^{1+}-dominated species in Cu-MTD.

Using ascorbic acid (AA) as a model substrate, we evaluated the oxidase-mimicking activities of Cu-MTD and Cu-AMTD through UV-vis spectra. In air-saturated pH-7.2 solution, AA presented an obvious absorption peak at 266 nm (Fig. 3A).[14] Once Cu-AMTD was introduced, the absorbance of the solution

Open Access Article. Published on 05 July 2025. Downloaded on 5/4/2026 11:46:44 PM.
This article is licensed under a Creative Commons Attribution-NonCommercial 3.0 Unported Licence.

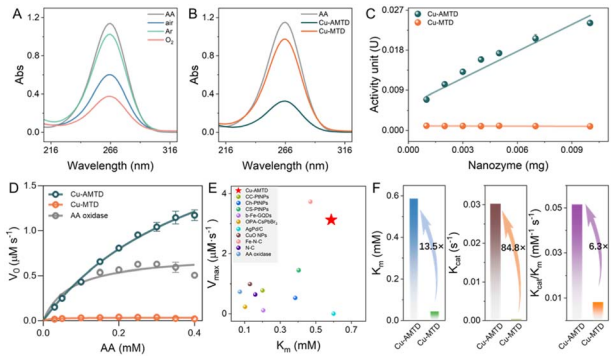

Fig. 3 Characterization of the AA-oxidase-mimicking activities of Cu-MTD and Cu-AMTD. (A) UV-vis spectra of AA catalyzed by Cu-AMTD in PBS solution; (B) UV-vis spectra of AA catalyzed by Cu-MTD and Cu-AMTD in air-saturated PBS solution; (C) specific activities; (D) Michaelis–Menten curves for AA; (E) a comparison of the catalytic activity of Cu-AMTD with reported AA-oxidase-like artificial enzymes and nanozymes; and (F) kinetic parameters (K_m, K_{cat} and K_{cat}/K_m).

notably decreased, demonstrating the oxidase-mimicking activity of Cu-AMTD. When the O_2 concentration increased, Cu-AMTD presented enhanced oxidase-like activity, which illustrated that Cu-AMTD was capable of catalyzing O_2 to oxidize AA. The catalytic activity of Cu-AMTD rose upon increasing the pH of the solution (Fig. S6†). To compare with reported AA oxidase-mimicking nanozymes under the optimal conditions,[15,16] a solution with a pH of 7.2 was chosen to evaluate the oxidase-mimicking activities of Cu-AMTD and Cu-MTD. According to UV-vis spectra, we observed negligible catalytic activity for Cu-MTD (Fig. 3B), and it was much lower than that of Cu-AMTD. This implied that modulating the mixed-valence Cu^{1+}/Cu^{2+} ratio *via* amino-induced S-bridge cleavage was crucial for boosting the AA oxidase-mimicking activity.

To further confirm the different oxidase-like performances of Cu-MTD and Cu-AMTD, we compared their specific and intrinsic activities. Fig. 3C displays that the specific activity of Cu-AMTD approached 2.0 U mg^{-1}, notably surpassing that of Cu-MTD. Upon increasing the initial concentration of AA, the catalytic rate of Cu-AMTD obviously rose, while Cu-MTD showed a negligible change in catalytic rate (Fig. 3D). Moreover, the catalytic rate of Cu-AMTD followed Michaelis–Menten kinetics (Fig. 3D). On the basis of the Lineweaver–Burk plot,[17–19] the corresponding apparent and intrinsic parameters such as V_{max}, K_m, K_{cat} and K_{cat}/K_m were further acquired through linear fitting (Fig. S7†). Fig. 3E and Table S2† reveal that the V_{max} value of Cu-AMTD not only surpassed that of Cu-MTD 68.6-fold but also rivalled most reported AA-oxidase-like nanozymes,[14–16,20–23] which indicated the superior oxidase-mimicking activity of Cu-AMTD. After soaking in aqueous solution for 79 h, the oxidase-like activity of Cu-AMTD did not obviously decrease, though its structure may change (Fig. S8†). Importantly, it can be seen that compared with Cu-MTD, Cu-AMTD exhibited much poorer affinity for AA, as confirmed by its 13.5-fold-lower K_m value (Fig. 3F). However, the K_{cat} and K_{cat}/K_m values of Cu-AMTD were 84.8- and 6.3-fold higher than those of Cu-MTD, respectively, which reflected the more rapid catalytic rate and efficiency of Cu-AMTD. The striking contrast was that the weaker affinity for AA instead provided Cu-AMTD with a faster rate of AA oxidation. This signified that the process of the oxygen reduction reaction (ORR) driven by O_2 adsorption and reductive activation over mixed Cu^{1+}/Cu^{2+} in Cu-AMTD may be more rapid compared with that over Cu-MTD, which contributed to enhancing the catalytic activity of Cu-AMTD.

To verify the above deduction, we compared the AA oxidation activities of Cu-MTD and Cu-AMTD in the absence of O_2. As seen in Fig. 4A, Cu-AMTD showed weaker electrocatalytic activity for AA oxidation compared with Cu-MTD. However, according to the catalytic kinetics experiment performed in the presence of O_2, AA oxidation over Cu-AMTD was actually more rapid than that over Cu-MTD (Fig. 3D). These results implied that the ORR process should be the key initial step for controlling the AA-oxidase-mimicking activity of Cu-AMTD rather than the step involving the oxidation of AA.

When the ORR process acted as the crucial initial step to trigger the AA-oxidase-like catalysis of Cu-AMTD, electron transfer followed the path of AA → Cu-AMTD → O_2 (Fig. 4B). If an extra reduction bias was applied to Cu-AMTD at this moment, another electron transfer path of electrode → Cu-AMTD → O_2 may occur in a competitive manner (Fig. 4B), which would generate an ORR current. A larger ORR current means stronger electron transfer through the electrode → Cu-AMTD → O_2 path, which would in turn make electron

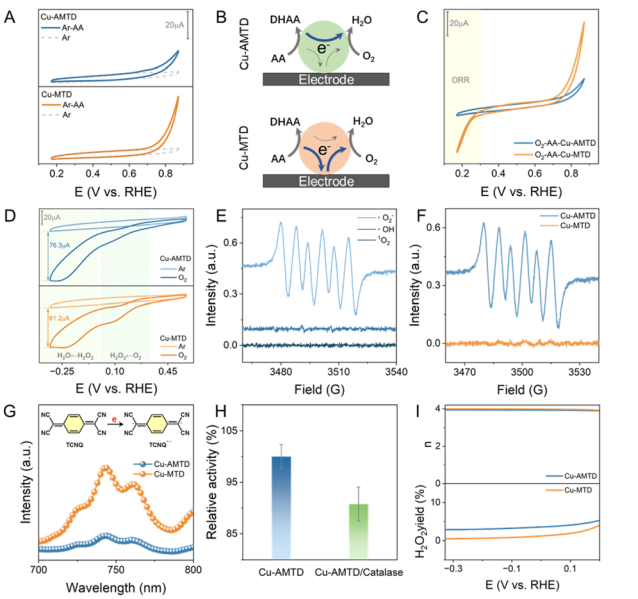

Fig. 4 (A) CV curves of Cu-MTD and Cu-AMTD in the absence and presence of AA under Ar; (B) a schematic illustration of electron transfer in the AA oxidation and O_2 reduction reactions; (C) CV curves of Cu-MTD and Cu-AMTD in the presence of AA under Ar and O_2; (D) CV curves of Cu-MTD and Cu-AMTD in the presence of Ar and O_2; (E) EPR spectra of Cu-AMTD for identifying $O_2^{\bullet-}$, $^{\bullet}OH$ and $^1O_2$; (F) EPR spectra of Cu-MTD and Cu-AMTD for a comparison of $O_2^{\bullet-}$; (G) UV-vis spectra of TCNQ solutions in the presence of Cu-MTD and Cu-AMTD; (H) specific trapping of H_2O_2 during the Cu-AMTD-catalyzed oxidation of AA using catalase; and (I) electron transfer numbers (n) and H_2O_2 yields of Cu-MTD and Cu-AMTD during the ORR.

© 2025 The Author(s). Published by the Royal Society of Chemistry

Open Access Article. Published on 05 July 2025. Downloaded on 5/4/2026 11:46:44 PM. This article is licensed under a Creative Commons Attribution-NonCommercial 3.0 Unported Licence.

transfer through the AA → Cu-AMTD → O_2 path weaker due to competitive effects between these two paths. According to Fig. 4C, we found that the ORR current presented by Cu-AMTD in the presence of O_2 was obviously lower than that presented by Cu-MTD. This illustrated that electron transfer through the AA → Cu-AMTD → O_2 path over Cu-AMTD was stronger than that over Cu-MTD, implying the faster ORR process of Cu-AMTD during catalysis. In cyclic voltammetry (CV) curves (Fig. 4D), the ORR current of Cu-AMTD was larger than that of Cu-MTD, supporting the stronger potential of Cu-AMTD for the reductive activation of O_2.

O_2 adsorption and activation in the initial step of the ORR generally generated $O_2^{\bullet-}$ and/or $^1O_2$. Thus, we performed electron paramagnetic resonance (EPR) experiments to analyze the reactive oxygen species (ROS) produced by Cu-MTD and Cu-AMTD. In theory, the more electron-deficient Cu^{2+} more easily adsorbed O_2 compared with Cu^{1+}. By contrast, Cu^{1+} was prone to donate an electron to O_2 due to its relatively more electron-rich characteristics. Thus, once O_2 was adsorbed on Cu^{2+}, the Cu^{1+} center adjacent to Cu^{2+} probably provided an electron to the adsorbed O_2 to form a ROS such as $O_2^{\bullet-}$. Based on the above speculation, the adjacent Cu^{2+} and Cu^{1+} in Cu-AMTD should make it easier to adsorb and activate O_2 to produce $O_2^{\bullet-}$ in the initial catalysis step, and the $O_2^{\bullet-}$ signal generated by Cu-MTD should be poor due to the rather low Cu^{2+} content. According to EPR spectra (Fig. 4E) collected in the absence of AA, we observed that Cu-AMTD generated a notable $O_2^{\bullet-}$ signal, and no $^1O_2$ species were detected for Cu-AMTD. Furthermore, compared with Cu-AMTD, the $O_2^{\bullet-}$ signal in the Cu-MTD system was much poorer and even negligible (Fig. 4F), which favored the idea that the mixed Cu^{1+}/Cu^{2+} in Cu-AMTD contributed to synergistically controlling the initial O_2 adsorption and reductive activation in the ORR process.

Once the Cu sites of Cu-AMTD adsorbed and activated O_2 into $O_2^{\bullet-}$ in the initial step of the ORR by donating an electron, Cu-AMTD should become more electron deficient, which would make Cu-AMTD become a better electron acceptor. To verify this, 7,7,8,8-tetracyanoquinodimethane (TCNQ) was subsequently employed as a probe molecule to determine the electron-accepting capabilities of Cu-AMTD. Fig. 4G shows that a peak at 743 nm was observed, which suggested that TCNQ accepted one electron from Cu-AMTD to form $TCNQ^{\bullet-}$.[24] However, this peak intensity of $TCNQ^{\bullet-}$ in the Cu-AMTD system was much lower than that in the Cu-MTD system, indicating the weaker electron-donation capabilities of Cu-AMTD. Generally speaking, stronger electron-donating abilities shown by a chemical species imply weaker electron-accepting abilities for that same species, and *vice versa*. In this sense, after the initial activation of O_2 to form $O_2^{\bullet-}$, Cu-AMTD became a better electron acceptor compared with Cu-MTD, which made it easier for Cu-AMTD to accept electrons from AA during mimicking AA-oxidase-like catalysis. As a result, this promoted the more-rapid oxidation of AA. All of the above results jointly indicated that the adjacent Cu^{1+}/Cu^{2+} centers of Cu-AMTD enhanced the activation of O_2 to $O_2^{\bullet-}$ in the initial step of the ORR through the synergistical mechanism of Cu^{2+}-dominated adsorption and Cu^{1+}-controlled electron transfer. After O_2 activation to produce $O_2^{\bullet-}$, Cu-AMTD generated more electron-deficient Cu sites, which subsequently accelerated AA oxidation, thereby boosting the AA-oxidase-mimicking activity of Cu-AMTD.

During mimicking AA-oxidase-like oxidation, the ORR process driven by Cu-AMTD experienced two obvious stages, corresponding to O_2 → H_2O_2 → H_2O,[8] as shown in Fig. 4A. To confirm the generation of the H_2O_2 intermediate, we performed trapping experiments using catalase, which could specifically identify H_2O_2. As displayed in Fig. 4H, adding catalase into the catalytic system resulted in an obvious decrease in the relative activity of Cu-AMTD, suggesting the generation of the H_2O_2 intermediate. Based on rotating ring-disk electrode (RRDE) measurements, the evaluated electron transfer number approaches 4 in the process of the Cu-AMTD-driven ORR (Fig. 4I), coinciding with the CV results (Fig. 4A). Moreover, according to the EPR spectra of Cu-AMTD, no $^{\bullet}OH$ signal was detected during mimicking AA-oxidase-like oxidation (Fig. 4E). On the basis of the detected reactive oxygen species, we proposed a possible catalytic mechanism (Fig. 5). During catalysis, Cu-AMTD preferentially adsorbed and activated O_2 to form $O_2^{\bullet-}$, which would be transformed into H_2O_2 by acquiring hydrogen atoms from AA and accepting electrons through the AA → Cu-AMTD → O_2 path, thus generating dehydroascorbic acid (DHAA). The formed H_2O_2 was further transformed into H_2O by obtaining electrons and hydrogen atoms from AA to generate H_2O and DHAA. Finally, the Cu centers of Cu-AMTD were regenerated by desorbing H_2O.

More-electron-deficient Cu generally possesses stronger coordination potential for P-containing compounds, which are common in flame retardants, pesticides and insecticides.[25–27] Thus, we further utilized this Cu-AMTD-driven oxidase-mimicking system to detect potentially cytotoxic tris(2-carboxyethyl)phosphine (TCEP),[28] which was chosen as a model P-based compound. As shown in Fig. 6A, introducing TCEP into this AA-oxidase-mimicking system promoted the absorbance of the solution containing AA to rebound, indicating the inhibition effect of TCEP on the catalytic system. Based on this inhibition effect, we determined the limit of detection (LOD) for TCEP to be 0.96 ppm by varying the TCEP content (Fig. 6B). This LOD for sensing TCEP was comparable to other sensing systems for detecting P-containing compounds

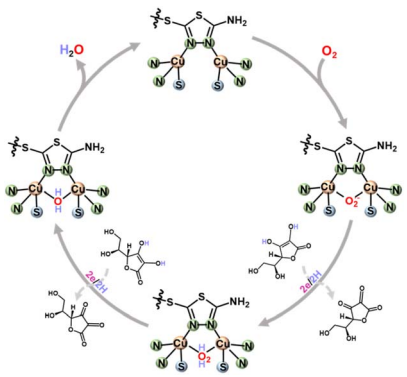

Fig. 5 The proposed catalytic mechanism of Cu-AMTD.

Open Access Article. Published on 05 July 2025. Downloaded on 5/4/2026 11:46:44 PM.
This article is licensed under a Creative Commons Attribution-NonCommercial 3.0 Unported Licence.

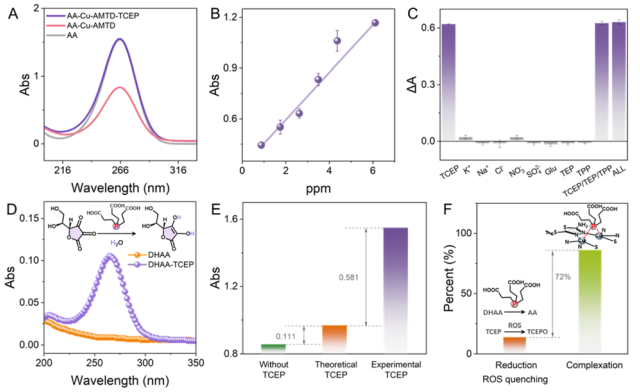

Fig. 6 The application of Cu-AMTD for the selective detection of TCEP. (A) UV-vis spectra of AA catalyzed by Cu-AMTD in the absence and presence of TCEP; (B) a linear plot of absorbance *versus* the concentration of TCEP; and (C) the selectivity of Cu-AMTD for detecting TCEP in the presence of interfering ions and molecules. (D) UV-vis spectra of DHAA in the absence and presence of TCEP; (E) a comparison of the theoretical and experimental absorbance of systems in the presence of 4.36-ppm TCEP; and (F) the contributions of reduction and complexation originating from TCEP toward inhibiting the catalytic activity of Cu-AMTD.

based on nanozymes, surface-enhanced Raman spectroscopy (SERS) and fluorescence (Table S3†).[29–31] Furthermore, we also found that the LOD for sensing TCEP in our nanozyme system was lower than a method using high-performance liquid chromatography coupled with evaporative light scattering detector (HPLC-ELSD), but higher than reported chemiluminescence and fluorescence systems (Table S3†).[32–35] Given that the structure and catalytic activity of our nanozyme was easy to adjust by modulating the structure of the ligand, there is still promise to further improve the LOD for TCEP sensing. Importantly, the Cu-AMTD-driven oxidase-mimicking system presented anti-interference capabilities toward inorganic ions (K^+, Na^+, Cl^-, SO_4^{2-} and NO_3^-), glucose (Glu), as well as other P-based flame-retardant compounds such as triethyl phosphate (TEP) and tripropyl phosphate (TPP) during detecting TCEP (Fig. 6C), thereby endowing this system with the potential for the selective detection of TCEP.

It was worth noting that from the viewpoint of structure, TPP and TCEP present similar molecular volumes, which signifies their similar steric effects (Fig. S9†). If steric effects played an important role in controlling the selective sensing of these organophosphorus compounds, TPP and TCEP should present similar inhibition effects on the catalytic activity of Cu-AMTD. However, Fig. 6C shows that the inhibition effect of TPP on the catalytic activity of Cu-AMTD was negligible compared with TCEP. This indicated that this selective sensing behavior of Cu-AMTD was not dependent on the steric effects of these organophosphorus compounds.

The EPR spectra displayed that introducing TCEP resulted in a notable decrease in the $O_2^{\bullet-}$ signal in the catalytic system (Fig. S10†), which may originate from the quenching of ROS and/or complexation-triggered inhibition effects. When mixing TCEP with the oxidation product of AA (*i.e.*, DHAA) in solution without adding Cu-AMTD, we found that TCEP was prone to reduce DHAA to generate AA (Fig. 6D). If assuming the inhibition effects of TCEP on the catalytic system totally stemmed from the quenching of ROS and the reduction potential of TCEP for the formed DHAA product, the calculated absorbance of this catalytic system should theoretically rise by 0.111 when adding 4.36-ppm TCEP (Fig. 6E). However, the experimentally obtained absorbance rose by 0.692 (Fig. 6E), far more than the theoretical value, which signified that the coordination effects of TCEP also participated in inhibiting the catalytic activity of Cu-AMTD. According to calculations, inhibition originating from complexation effects and the reduction/ROS quenching potential of TCEP accounted for 86% and 14%, respectively (Fig. 6F). These results indicated that differences in the electronic structures and resulting affinities of these detected species for the copper sites endowed Cu-AMTD with the observed high selectivity towards TCEP over other tested organophosphorus compounds as well as ionic species.

Conclusions

In summary, a thiadiazole-coordinated Cu nanozyme system was developed by modulating the side group of the thiadiazole ligand to disclose the roles of the mixed Cu^{1+}/Cu^{2+} centers in controlling the oxidase-like activity. The introduction of an amino group into the thiadiazole ligand triggered the cleavage of the electron-communicating S-bridge between adjacent dicopper centers. As a result, this modulated the ratio of mixed Cu^{1+}/Cu^{2+} sites, which synergistically control O_2 adsorption and electron transfer to accelerate the selective activation of O_2 to $O_2^{\bullet-}$ in the initial step of the ORR. Such enhanced production of $O_2^{\bullet-}$ further endowed the resulting Cu-based nanozyme (Cu-AMTD) with superior oxidase-like activity, far surpassing the control nanozyme with S-bridged Cu centers (Cu-MTD). Moreover, the mixed Cu^{1+}/Cu^{2+} sites in Cu-AMTD showed excellent affinity for cytotoxic TCEP, thereby enabling this nanozyme to exhibit high selectivity and a low LOD during TCEP sensing. Our findings not only provided fundamental insight into the mixed-valence synergy of metal sites for nanozyme catalysis, but also offered a novel ligand engineering strategy to manipulate the mixed-valence states of metal sites for developing advanced catalysts for a broad spectrum of applications beyond catalysis and sensing.

Data availability

The data that support the findings of this study are available in the ESI.†

Author contributions

F. H. conceived and designed the experiments. B. L. performed the synthesis and/or activity evaluation of nanozymes. N. X. and C. H. provided help with applying for the funding. F. H. wrote and revised the manuscript. F. H. and X. H. supervised the project.

© 2025 The Author(s). Published by the Royal Society of Chemistry

Open Access Article. Published on 05 July 2025. Downloaded on 5/4/2026 11:46:44 PM. This article is licensed under a Creative Commons Attribution-NonCommercial 3.0 Unported Licence.

Conflicts of interest

The authors declare no competing financial interests.

Acknowledgements

This work was financially supported by National Natural Science Foundation of China (No. 52276195), Doctoral Fund Project of University of Jinan (XBS2409), Opening Project of State Key Laboratory Incubation Base for Green Processing of Chemical Engineering (Shihezi University, China), the Foundation (No. GZKF202335) of State Key Laboratory of Biobased Material and Green Papermaking (Qilu University of Technology, Shandong Academy of Sciences), Program for supporting innovative research from Jinan (202228072) and Program of agricultural development from Shandong (SD2019NJ015). The authors extend their gratitude to Mr Yanda Du from Shiyanjia Lab (**https://www.shiyanjia.com**) for providing invaluable assistance with the XPS analysis.

Notes and references

1 Y. Xu, Y. Ma, X. Chen, K. Wu, K. Wang, Y. Shen, S. Liu, X. J. Gao and Y. Zhang, *Angew. Chem.*, 2024, **136**, e202408935.
2 X. Wang, M. Liu, Y. Liu, X. Zhang, L. Li, X. Xue, M. Humayun, H. Yang, L. Sun, M. Bououdina, J. Zeng, D. Wang, R. Snyders, D. Wang and C. Wang, *Angew. Chem.*, 2025, e202504923.
3 D. Chen, Z. Xia, Z. Guo, W. Gou, J. Zhao, X. Zhou, X. Tan, W. Li, S. Zhao, Z. Tian and Y. Qu, *Nat. Commun.*, 2023, **14**, 7127.
4 S. Zhang, X. J. Gao, Y. Ma, K. Song, M. Ge, S. Ma, L. Zhang, Y. Yuan, W. Jiang, Z. Wu, L. Gao, X. Yan and B. Jiang, *Nat. Commun.*, 2024, **15**, 10605.
5 M. Li, J. Chen, W. Wu, Y. Fang and S. Dong, *J. Am. Chem. Soc.*, 2020, **142**, 15569–15574.
6 M. Sha, L. Rao, W. Xu, Y. Qin, R. Su, Y. Wu, Q. Fang, H. Wang, X. Cui, L. Zheng, W. Gu and C. Zhu, *Nano Lett.*, 2023, **23**, 701–709.
7 M. Yuan, N. Xia, X. Hu and F. He, *Small*, 2024, **20**, 2403850.
8 M. Yuan, N. Xia, Z. Huang, C. Huang, X. Hu and F. He, *Chem. Sci.*, 2024, **15**, 19513–19519.
9 X. Zhang, L. Lu, A. Luo, W. Xiong and J. Chen, *Appl. Surf. Sci.*, 2023, **611**, 155703.
10 M. Balamurugan, H.-Y. Jeong, V. S. K. Choutipalli, J. S. Hong, H. Seo, N. Saravanan, J. H. Jang, K.-G. Lee, Y. H. Lee, S. W. Im, V. Subramanian, S. H. Kim and K. T. Nam, *Small*, 2020, **16**, 2000955.
11 Z. Wang, H.-I. Un, T.-J. Liu, B. Liang, M. Polozij, M. Hambsch, J. F. Pöhls, R. T. Weitz, S. C. B. Mannsfeld, U. Kaiser, T. Heine, H. Sirringhaus, X. Feng and R. Dong, *Angew. Chem.*, 2025, **137**, e202423341.
12 M. Joglekar, S. Pylypenko, M. M. Otting, J. S. Valenstein and B. G. Trewyn, *Chem. Mater.*, 2014, **26**, 2873–2882.
13 J.-P. Piquemal, J. Maddaluno, B. Silvi and C. Giessner-Prettre, *New J. Chem.*, 2003, **27**, 909–913.
14 X. Cao, C. Zhu, Q. Hong, X. Chen, K. Wang, Y. Shen, S. Liu and Y. Zhang, *Angew. Chem.*, 2023, **135**, e202302463.
15 S. He, A. Hu, Q. Zhuang, H. Peng, H. Deng, W. Chen and G. Hong, *ChemBioChem*, 2020, **21**, 978–984.
16 H. Fan, W. Yang, Y. Dai, L. Huang, Q. Zhang, H. Zhang, J. Liu, W. Zhu and J. Hong, *Anal. Chim. Acta*, 2024, **1318**, 342931.
17 G. Li, H. Liu, T. Hu, F. Pu, J. Ren and X. Qu, *J. Am. Chem. Soc.*, 2023, **145**, 16835–16842.
18 S. Xu, H. Wu, S. Liu, P. Du, H. Wang, H. Yang, W. Xu, S. Chen, L. Song, J. Li, X. Shi and Z. G. Wang, *Nat. Commun.*, 2023, **14**, 4040.
19 T. Li, X. Wang, Y. Wang, Y. Zhang, S. Li, W. Liu, S. Liu, Y. Liu, H. Xing, K. Otake, S. Kitagawa, J. Wu, H. Dong and H. Wei, *Nat. Commun.*, 2024, **15**, 10861.
20 S.-B. He, L. Yang, Y. Yang, H. A. A. Noreldeen, G.-W. Wu, H.-P. Peng, H.-H. Deng and W. Chen, *Carbohydr. Polym.*, 2022, **298**, 120120.
21 S. B. He, L. Yang, M. T. Lin, H. A. A. Noreldeen, R. X. Yu, H. P. Peng, H.-H. Deng and W. Chen, *Sens. Actuators, B*, 2021, **347**, 130627.
22 Q. Ye, E. Yuan, J. Shen, M. Ye, Q. Xu, X. Hu, Y. Shu and H. Pang, *Adv. Sci.*, 2023, **10**, 2304149.
23 L. Luo, J. Liu, Y. Liu, H. Chen, Y. Zhang, M. Liu and S. Yao, *Food Chem.*, 2024, **430**, 137062.
24 J. Song, Z. Ji, Q. Nie and W. Hu, *Nanoscale*, 2014, **6**, 2573–2576.
25 P. Mei, Z. Ma, Y. Chen, Y. Wu, W. Hao, Q. H. Fan and W. X. Zhang, *Chem. Soc. Rev.*, 2024, **53**, 6735–6778.
26 S. Naveen Prasad, V. Bansal and R. Ramanathan, *TrAC, Trends Anal. Chem.*, 2021, **144**, 116429.
27 D. Song, T. Tian, X. Yang, L. Wang, Y. Sun, Y. Li and H. Huang, *Food Chem.*, 2023, **424**, 136477.
28 I. Koh, I. Yong, B. Kim, D. Choi, J. Hong, Y.-M. Han and P. Kim, *ACS Biomater. Sci. Eng.*, 2020, **6**, 813–821.
29 X. Yan, H. Li, Y. Yan and X. Su, *Food Chem.*, 2015, **173**, 179–184.
30 J. Sun, L. Gong, Y. Lu, D. Wang, Z. Gong and M. Fan, *Analyst*, 2018, **143**, 2689–2695.
31 X. Ma, J. Xie, Z. Wang and Y. Zhang, *Spectrochim. Acta, Part A*, 2022, **267**, 120542.
32 Z. Tan, P. M. Ihnat, V. S. Nayak and R. J. Russell, *J. Pharm. Biomed. Anal.*, 2012, **59**, 167–172.
33 H. Guo, W. Tang and X. Duan, *Anal. Methods*, 2018, **10**, 5823–5826.
34 M. Saqib, S. Bashir, H. Li, S. Wang and Y. Jin, *Anal. Chem.*, 2019, **91**, 3070–3077.
35 T. Shu, J. Wang, L. Su and X. Zhang, *Anal. Chem.*, 2016, **88**, 11193–11198.

© 2025 The Author(s). Published by the Royal Society of Chemistry